*lubricants*

MDPI

*Article*

# Fabricating Laser-Induced Periodic Surface Structures on Medical Grade Cobalt–Chrome–Molybdenum: Tribological, Wetting and Leaching Properties

**Sanne H. van der Poel [1,†], Marek Mezera [2,†], Gert-willem R. B. E. Römer [2], Erik G. de Vries [1] and Dave T. A. Matthews [1,*]**

[1] Chair of Surface Technology and Tribology, Department of Mechanics of Solids, Surfaces and Systems (MS3), Faculty of Engineering Technology, University of Twente, Drienerlolaan 5, 7522 NB Enschede, The Netherlands

[2] Chair of Laser Processing, Department of Mechanics of Solids, Surfaces and Systems (MS3), Faculty of Engineering Technology, University of Twente, Drienerlolaan 5, 7522 NB Enschede, The Netherlands

* Correspondence: d.t.a.matthews@utwente.nl

† These authors contributed equally to this work.

Received: 12 July 2019; Accepted: 8 August 2019; Published: 13 August 2019


**Abstract:** Hip-implants structured with anti-bacterial textures should show a low-friction coefficient and should not leach hazardous substances into the human body. The surface of a typical material used for hip-implants, namely Cobalt–Chrome–Molybdenum (CoCrMo) was textured with different types of laser-induced periodic surface structures (LIPSS)—i.e., low spatial frequency LIPSS (LSFL), hierarchical structures consisting of grooves superimposed with high spatial frequency LIPSS (HSFL) and Triangular shaped Nanopillars (TNP)—using a picosecond pulsed laser source. The effect of LIPSS on the wettability, friction, as well as wear of the structures, when slid against a polyethylene (PE) counter surface and biocompatibility was analyzed. Surfaces covered with LSFL show superhydrophobicity and grooves with superimposed HSFL, as well as TNP, show hydrophobic behavior. The coefficient of friction (CoF) of LIPSS against a polyethylene (PE) counter surface was found to be higher (ranging from 0.40 to 0.66) than the CoF of (polished) CoCrMo, which was found to equal 0.22. It was found that the samples release cobalt within biocompatible limits. Compared to polished reference surfaces, LIPSS cause higher friction of CoCrMo against PE contact. However, the wear of the PE counter surface only increased significantly for the LSFL textures. For these reasons, it is concluded that LIPSS are not suitable for a heavily loaded metal-on-plastic bearing contact.

**Keywords:** CoCrMo; LIPSS; LSFL; HSFL; grooves; triangular LIPSS

## 1. Introduction

At least 3% of the patients that require primary total hip arthroplasty surgery need a revision due to severe prosthetic joint infections [1]. This leads to additional hospitalizations, costs and compromises the patient's health. Surface textures in the nano- and micrometer scale are observed in nature, that have an antibacterial effect, such as butterfly wings and shark skin [2]. Anti-bacterial surface features must be of the same order or slightly smaller than the bacteria size, in order to influence the adherence behavior of the bacteria [3]. This effect is based on the reduction of the amount of available surface for the bacteria cell to adhere to. Bacteria that most often cause prostheses related infections are *Staphylococcus aureus* and *Escherichia coli* [4]. The characteristic dimensions of the bacteria are one to three μm in diameter [5,6].

Cobalt–Chrome–Molybdenum (CoCrMo) is an alloy that is most often used for the bearing surface of a hip implant, due to its high fatigue, wear and corrosion resistance [7]. In a metal-on-plastic artificial hip joint, the CoCrMo femur head articulates against an polyethylene (PE) acetabulum cup. The surface of the CoCrMo component is traditionally mirror polished [8].

An established method to alter surface properties on the nano- to micrometer scale is laser surface texturing using (ultra-) short laser pulses. Under specific conditions, this can lead to so called laser-induced periodic surface structures (LIPSS). LIPSS are nanometer sized, regular patterned surface textures and can improve tribological performance [9,10], wettability properties [10–15], anti-bacterial properties [15–18] and cell-tissue growth [11].

In order to reduce infections, LIPSS having dimensions (periodicity and amplitude) about the size of the bacterias on the CoCrMo material could improve the antibacterial performance of the CoCrMo femur. However, hip-implants also should show a low-friction coefficient and should not leach hazardous materials into the human body. Therefore, the aim of this study is to not only study the formation of LIPSS on CoCrMo, but also study the tribological properties of CoCrMo on PE as well as the wettability and the leaching properties of the textures. In this study, a picosecond pulsed laser is used to create different types of LIPSS on CoCrMo surfaces. To the best of the authors knowledge, it is the first report of hexagonally packed triangular nanopillar LIPSS produced with a picosecond laser on CoCrMo. The tribological, wetting and leaching properties of different types of LIPSS on CoCrMo are investigated and compared.

## 2. Materials and Methods

### *2.1. Laser Setup and Material*

Figure 1a shows the experimental laser setup schematically. It consists of a pulsed Yb:YAG disk laser source (TruMicro 5050 of Trumpf GmbH, Ditzingen, Germany) emitting a laser beam with a wavelength of 1030 nm, maximum pulse frequency of 400 kHz, pulse energies up to 125 µJ and a fixed pulse duration of 6.7 ps. The fluence profile of the focal laser spot is nearly Gaussian ($M^2 < 1.3$). The polarization of the laser beam exiting the laser head is linear. Besides exposing the material to linear laser polarization, also a quarter wave plate was included in the setup to achieve circular polarization, which may lead to triangular shaped LIPSS textures. The beam was focused on the surface of the samples, using a telecentric F$\theta$ lens (Ronar of Linos GmbH, Göttingen, Germany) with a focal length of 80 mm, resulting in a focal spot with an $e^{-2}$-diameter of $d = 33.6 \pm 1.6$ µm (see Section 2.2.1).

The samples consists of polished CoCrMo discs with a diameter of 25 mm and a thickness of 3 mm. The surface roughness ($R_a = 0.003 \pm 0.0003$ µm, $R_q = 0.004 \pm 0.0004$ µm) of the discs was measured with an atomic force microscope (NX10, Park Systems Corp., Suwon, South Korea). manufacturer's headquarters. The beam was scanned over the substrate using a galvoscanner (intelliSCAN14 of ScanLab GmbH, Puchheim, Germany) at normal incidence in air, see Figure 1b. Different shapes and sizes of LIPSS were produced by adjusting the type of polarization (linear or circular) and by adjusting the laser peak fluence ($F_0$) and the number of overscans of the laser spot over the surface ($N_{OS}$). The scan velocity of the laser spot ($v$), the laser pulse frequency ($f_F$) and the spatial pitch between laser pulses on the surface ($\Delta x, \Delta y$) were kept constant in this study at $v = 2$ m/s, $f_F = 1000$ Hz and $\Delta x = \Delta y = 5$ µm, respectively, see Figure 1b. This yields a geometrical pulse-to-pulse overlap (OL) in both, $x$- and $y$-direction, of $OL = 1 - v/(d \cdot f_F) \approx 0.85$. All samples were cleaned in an ultrasonic bath with ethanol for 20 min and dried in ambient air after laser treatment. Table 1 shows the chemical composition of the samples.

**Table 1.** Cobalt–Chrome–Molybdenum (CoCrMo) alloy composition in weight percent, the composition is balanced (Bal.) with Cobalt.

| Element | Co | Cr | Mo | Ni | Si; Mn; Fe |
|---|---|---|---|---|---|
| wt % | Bal. | 27 – 30 | 5 – 7 | ≤2 | ≤1 |

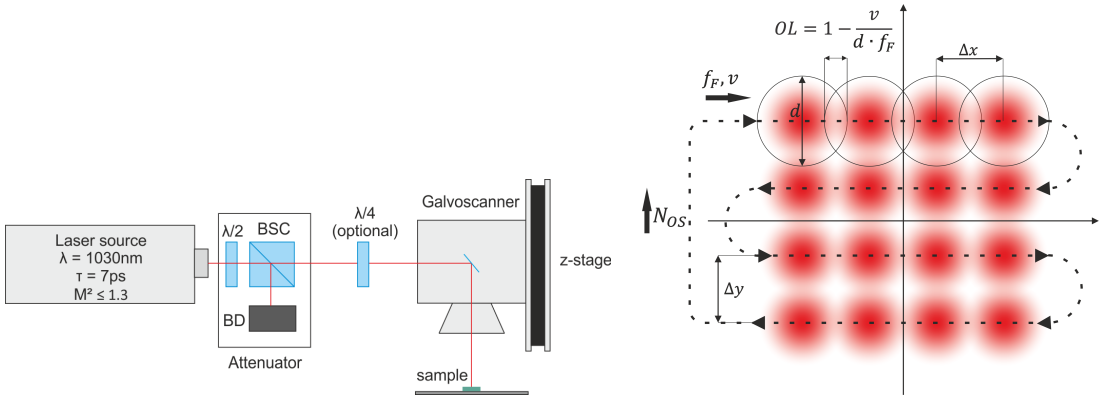


**Figure 1.** Schematic representations of the laser setup and the scanning trajectory of the laser spot. (**a**) Schematic representation of the laser setup; $\lambda/2$: half-wave plate; BSC: beam splitter cube; BD: beam dump; $\lambda/4$: quarter-wave plate (optional). (**b**) Scanning trajectory of the laser spot; $f_F$: pulse frequency; $v$: scan velocity; $d$: beam diameter; $OL$: geometrical pulse-to-pulse overlap; $N_{OS}$: number of overscans; $\Delta x$, $\Delta y$: geometrical pitch between subsequent laser pulses in $x$- and $y$-direction.

## 2.2. Analysis Tools

### 2.2.1. Laser Beam Characterization

The laser power was measured using an thermopile power sensor (PM30 of Coherent, Santa Clara, CA, USA) with a measurement uncertainty of ±1%, connected to a readout unit (FieldMaxII-TOP of Coherent, Santa Clara, CA, USA). The focal spot diameter 33.6 ± 1.6 µm ($e^{-2}$) was measured using a laser beam characterization device (MicroSpotMonitor of Primes GmbH, Pfungstadt, Germany).

### 2.2.2. Surface Morphology Dimensions

Laser-induced surface structures were analyzed using a scanning electron microscope (JSM-7200F, Jeol, Tokyo, Japan). From SEM micrographs, the periodicity of LIPSS areas were analyzed with the help of a 2D fast Fourier transform (FFT) algorithm using a MATLAB [19] script. Details of the script are reported in our earlier work [20].

The roughness of the surface textures was analyzed by means of an atomic force microscopy (NX10, Park Systems Corp., Suwon, South Korea) in true non-contact™ mode using a non-contact cantilever (PPP-NCHR, 125 × 30 × 4 µm, Tip < 10 nm, Park Systems Corp., Suwon, South Korea). The roughness parameters that were extracted from these measurements are used to characterize the surface by means of root mean square surface area roughness ($R_q$), average surface area roughness ($R_a$), maximum peak height ($R_p$), maximum valley depth ($R_v$), skewness ($R_{sk}$), kurtosis ($R_{ku}$) and the ratio between the real surface area and the projected area ($\sigma$).

### 2.2.3. Contact Mechanism and Friction Parameters

The wear of the samples was characterized in a wear test in which the textured sample was exposed to a polyehtylene (PE) ball (diameter of 9.5 mm) sliding over the surface in BCS as lubricant, in order to simulate the human body environment. The sample discs are clamped in a Universal Mechanical Tester (UMT, Bruker, Billerica, MA, United States). The PE ball was pressed against

the sample surface and moved in a reciprocate fashion for 104 min with 11 mm/s and a normal load of 0.5 N (18 MPa contact pressure) [21]. The normal force and the shear force are measured and the coefficient of friction during steady state of the wear test was calculated. The wear of the PE ball surface is analyzed by observing the wear diameter with a confocal microscope (S Neox, Sensofar, Terassa, Spain). The wear of the textures is investigated with a SEM (see Section 2.2.2) and energy-dispersive X-ray spectroscopy (EDS) analysis in the same SEM system.

#### 2.2.4. Contact Angle Measurement

The wettability of the textures was characterized by means of a contact angle measurement device (SCA20, DataPhysics Instruments GmbH, Filderstadt, Germany). The sample surfaces were wiped with isopropanol and dried under ambient conditions prior to analysis. Next, a droplet of water of 5 µL was deposited on the surface and the angle between the surface and the droplet was measured. Three measurements were conducted for each sample.

#### 2.2.5. Biocompatability

The substrates were sterilized by immersing them in ethanol for 15 min. A simulated body fluid (SBF) solution was made according to the instructions of Kokubo et al. [22]. That is, salts were dissolved in de-ionized water such that a solution was created with ion concentrations similar to that of blood plasma. The pH value of SBF (7.40) is comparable to the pH of human blood plasma, which ranges from 7.2 to 7.4. The substrates were immersed in 40 mL of SBF solution at 37 °C in a shaking incubator (160 rpm). The ion release was analyzed after 1, 7, 14, 21 and 26 days respectively. Inductively Coupled Plasma Atomic Emission Spectroscopy (ICP-AES) (Optima 5300 dual view, PerkinElmer Inc., Waltham, MA, USA) was used to analyze the leaching properties.

## 3. Results and Discussion

### *3.1. Surface Structures Processed with Linear Polarization*

Two types of surface textures were processed using linear polarized laser irradiation, by applying increasing peak fluence levels and various number of overscans during the laser processing. These two types are low spatial frequency LIPSS (LSFL, see Figure 2) and hierarchical structures composed of micro-grooves and superimposed LSFL (see Figure 3).

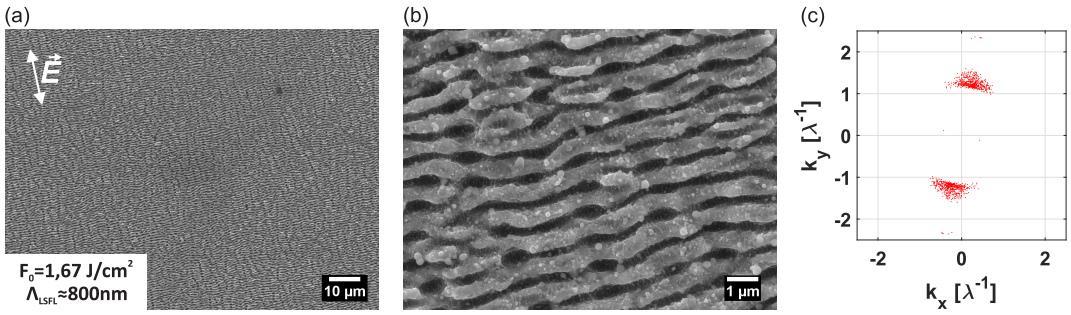


**Figure 2.** Scanning electron microscope (SEM) micrographs of low spatial frequency laser-induced periodic surface structures (LSFL) processed on CoCrMo with a laser peak fluence of $F_0 = 1.67$ J/cm$^2$ and number of overscans $N_{OS} = 1$ ((**a**) 1000× magnification; and (**b**) 10,000× magnification). (**c**) 2D-fast Fourier transform (FFT) map of the SEM micrograph (**a**). The spatial periodicity of the LSFL is $\Lambda \approx 800$ nm. The arrow in micrograph (**a**) indicates the direction of the E-field of the laser polarization.

The periodicity of the LSFL in Figure 2 was found to equal $\Lambda \approx 800$ nm and are perpendicular to the E-field of the laser polarization direction, which is typical for LSFL on metals [23]. LSFL on the sample are spread homogeneously over the processed surface of $5 \times 5$ mm$^2$.

Figure 3 shows SEM micrographs of hierarchical structures processed on CoCrMo with $N_{OS} = 5$ and various peak fluence levels. It can be observed in this figure, that with increasing peak fluence levels, the periodicity of the micro grooves increases from $\Lambda_{Grooves} \approx 3.55$ µm at a peak fluence level of $F_0 = 1.82$ J/cm$^2$ to $\Lambda_{Grooves} \approx 7.9$ µm at $F_0 = 7.07$ J/cm$^2$. The formation of micro-grooves and micro-bumps is attributed to an increased heat accumulation during processing [24–26].

The periodicity $\Lambda_{LSFL} \approx 920$ nm of the LSFL in Figure 3 was constant for all fluence levels within the fluence range studied. It is known that the LSFL periodicity increases with increasing fluence levels up to a certain fluence level, after which the periodicity does not vary with the fluence [27,28].

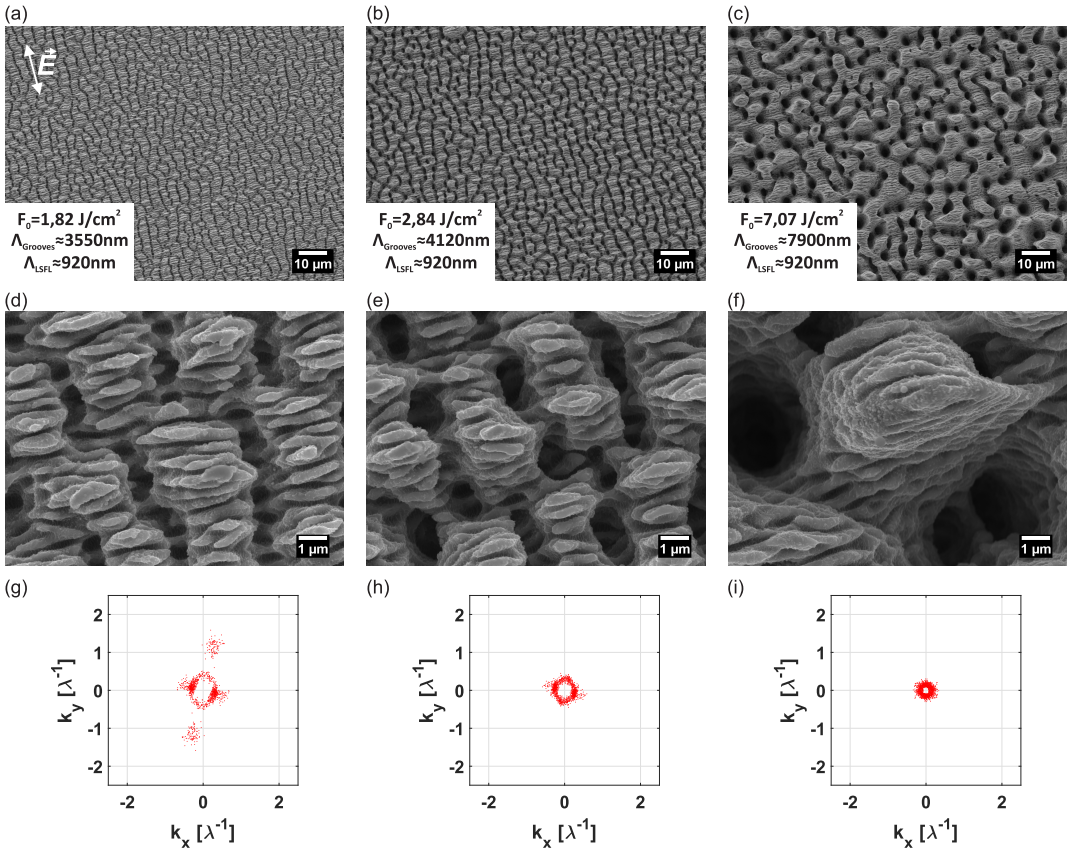


**Figure 3.** SEM micrographs of hierarchical structures processed on CoCrMo with $N_{OS} = 5$ and various peak fluence levels at two different magnifications ((**a**–**c**) 1000×; and (**d**–**f**) 10,000×). (**g**–**i**) 2D-FFT maps of the micrographs of the processed areas (**a**–**c**). The periodicity of the micro-grooves $\Lambda_{Grooves}$ increases with increasing peak fluence levels. The periodicity of the LSFL features are constant at $\Lambda_{LSFL} \approx 920$ nm for all micrographs. The arrow in micrograph (**a**) indicates the direction of the E-field of the laser polarization.

### *3.2. Surface Structures Processed with Circular Polarization*

Triangular nanopillars (TNP), hexagonally packed, can be produced by exposing the surface to either circular polarized ultra-short laser pulses [13], or to double-pulsed (bursts of pulses), linear cross-polarized, ultra-short laser pulses [29,30]. These types of structures might be preferred over LSFL for the aimed application, since TNP are symmetric in three directions, whereas LSFL are symmetric in only one direction. Because hip joints rotate with respect to the $x$-, $y$- and $z$-axis, the tribological characteristics of the bearing should ideally be equal in any direction.

The physical phenomena behind the formation of triangular LIPSS are still under debate [13,29,30]. e.g., Fraggelakis et al. [30] proposes that the convection flow of the molten material layer as a cause for this type of LIPSS, whereas Liu et al. [29] claims the 2D nanotriangle structures develop due to the interference of surface plasmon polaritons (SPP's) with the incoming laser light. Since Liu et al.

applied cross-polarized, time delayed double-pulses, these authors argue that the first pulse induces SPP's and the interference with the laser light leads to transient, spatially periodic meta-gratings of a modified refractive index on the surface with a wave vector parallel to the laser polarization. Further, they claim that the second cross-polarized pulse also induces SPP's at the surface due to surface roughness with a wave vector parallel to the laser polarization. The latter SPP then interferes with the transient refractive index meta grating of the first pulse and could diffract into two SPP's with different wave vectors. The interference of the laser light with these three SPP's in different directions leads to ablation of a hexagonal pattern, resulting in triangular shaped nanostructures.

Figure 4 shows SEM micrographs of surface structures processed on CoCrMo with circular polarization with $N_{OS} = 1$ and increasing peak fluence levels. It can be observed from Figure 4a, that LSFL with a periodicity of about $\Lambda_{LSFL} \approx 860$ nm form at a peak fluence level of $F_0 = 2.87$ J/cm$^2$. This structure may be an indication that the polarization is not perfectly circular, but actually elliptically polarized with the main axis perpendicular to the processed LSFL. It can also be observed in Figure 4a, that "interruptions" of the LSFL features start to appear in the direction and the periodicity of the hexagonal shapes, see Figure 4a and the indicated frequencies on the 2D-FFT map of Figure 4a. Further it can be recognized when comparing Figure 4a,b, that these "interruptions" are indeed a surface morphology "proceeding" the formation of grooves in two different directions, which then form the triangular nanopillars if the fluence is increased. At a fluence level of $F_0 = 5.23$ J/cm$^2$, regular TNP are formed, which become less regular and less pronounced for higher fluence levels, see Figure 4c. When comparing the laser processing conditions and groove periodicities between the hexagonal nanopillars with earlier studies (see Table 2), it becomes evident, that the hexagonal pattern processed either with single pulses of circular polarization or with cross polarized pulses with linear polarization origin from the same physical phenomena. Hence, the physical explanation of the origin for those patterns has to apply for each case of laser processing condition listed in Table 2. The physical explanation of hexagonal nanopillars exceeds the scope of this paper.

**Table 2.** Comparison of laser processing parameters and groove periodicity of hexagonal nanostructures with earlier studies.

| Wavelength [nm] | Pulse Duration | Pulse Frequency [kHz] | Polarization | Period between Grooves | Reference |
|---|---|---|---|---|---|
| 1030 | 7 ps | 400 | Circular, non-burst pulses | 0.83 $\lambda$ | This study |
| 1032 | 310 fs | 250 | Circular, non-burst pulses | 0.84–0.98 $\lambda$ | [13] |
| 710 | 50fs | 1 | Linear, cross-polarized bursts of pulses | 0.89 $\lambda$ | [29] |
| 1030 | 350 fs | 100 | Circular, opposite direction of rotation & Linear, cross-polarized bursts of pulses | 0.85 $\lambda$ | [30] |

High spatial frequency LIPSS (HSFL) were found between the formed LSFL in Figure 4a and the triangular nanopillars in Figure 4b,c, with a periodicity of $\Lambda_{HSFL} \approx 80$ nm. Liu et al. [29] processed triangular nanopillars with two consecutive, cross-polarized pulses with a pulse duration of 50 fs and with a time delay of 1.2 ps on tungsten in air and in vacuum. In the latter study, HSFL were not observed when processing tungsten in air, but have been observed when processing tungsten at low pressures of $10^{-3}$ Pa. It was claimed, that the formation of HSFL is attributed to a slower cooling rate of the molten, liquid material layer at lower pressures. In the latter case, less air exists in the experimental environment, to transfer the heat from the molten layer to. Therefore, heat remains in the molten layer for a longer period of time and the cooling rate decreases. Thus, when the liquid material cools down, there is more time for shrinking and film fragmentation of the melt into HSFL then when processing in air. Compared to the latter study, the pulse duration of the laser used in this work, is in the order of two magnitudes larger. Hence, more heat is introduced into the lattice, which might explain the occurrence of HSFL between LSFL and triangular nanopillars when processed in air.

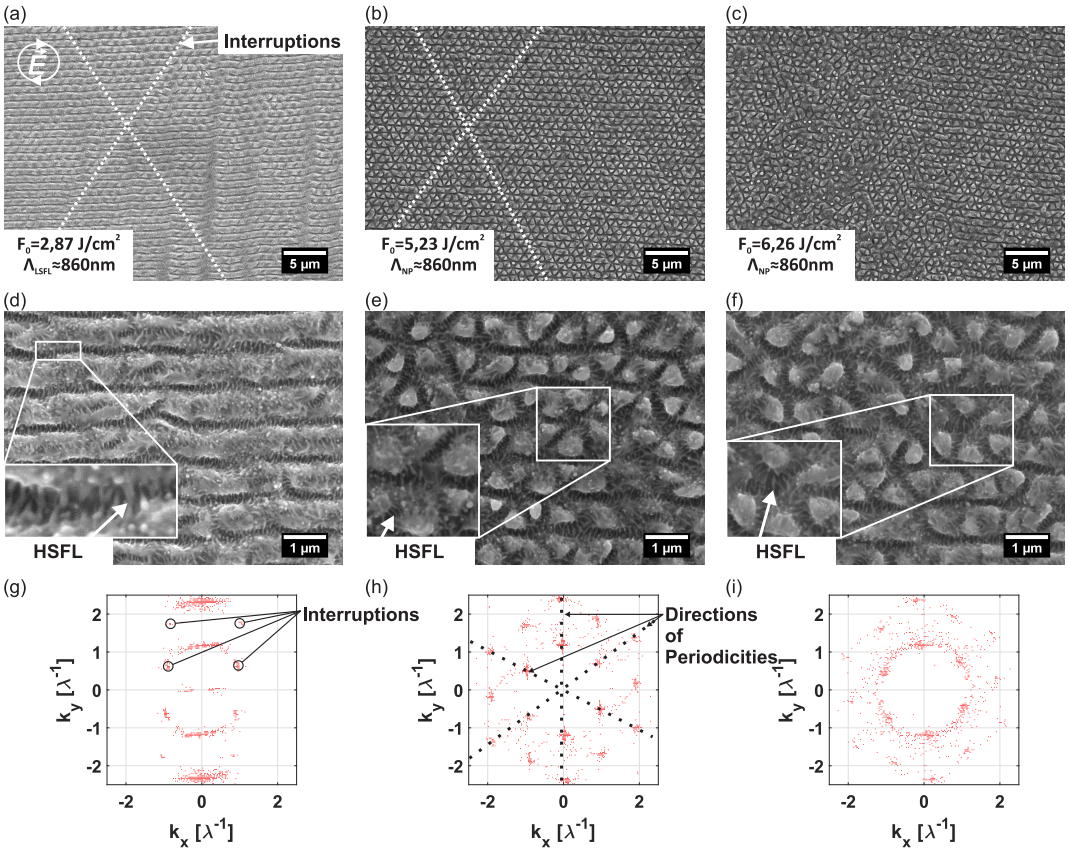


**Figure 4.** SEM micrographs of surface structures processed on CoCrMo using circular polarized laser radiation at $N_{OS} = 1$ and various peak fluence levels at two different magnifications ((**a**–**c**) 3000×; and (**d**–**f**) 15,000×). (**g**–**i**) 2D-FFT maps if the micrographs of the processed areas (**a**–**c**). The periodicity of the LSFL in (**a**) is about $\Lambda_{LSFL} \approx 860$ nm. The periodicity of the nanopillars is constant in the same range $\Lambda_{TNP} \approx 860$ nm. The arrow in micrograph (**a**) indicates the direction of the E-field of the laser polarization.

### *3.3. Surface Morphology Dimensions*

Three laser-textured surface patterns were chosen, based on their morphologies and uniformity, for the study of wettability properties, tribological performance and anti-bacterial behavior, see Figure 5. The laser parameters used to create these structures are listed in Table 3.

**Table 3.** Surface structures to be functionally evaluated processed with a pulse frequency of $f = 400$ kHz and a laser scanning velocity of 2 m/s.

| Texture | Structure Types | Peak Fluence $F_0$ (J/cm$^2$) | $N_{OS}$ | Laser Polarization | Figure |
|---|---|---|---|---|---|
| LSFL | LSFL | $1.67 \pm 0.01$ | 1 | linear | 2a,b, 5b |
| Grooves | Grooves + LSFL | $2.84 \pm 0.01$ | 5 | linear | 3a,d, 5c |
| TNP | hexagonal Nanopillars + HSFL | $5.23 \pm 0.01$ | 1 | circular | 4b,e, 5d |

The roughness parameters of these surface textures are listed in Table 4. As can be concluded from this table, the roughness parameters of these surfaces vary. Hence, significant differences in the functional properties (wetting, wear, biocompatibility) of these textures are expected. The higher value of $R_a$ indicate that Grooves are more rough than a surface covered with only LSFL. Compared to the polished CoCrMo surface, the square root surface roughness $R_q$ increases significantly due to laser-texturing. Quantitavely, 23 times $R_q^{polished}$ in the case of nanopillars and up to 130 times $R_q^{polished}$ in the case of grooves.

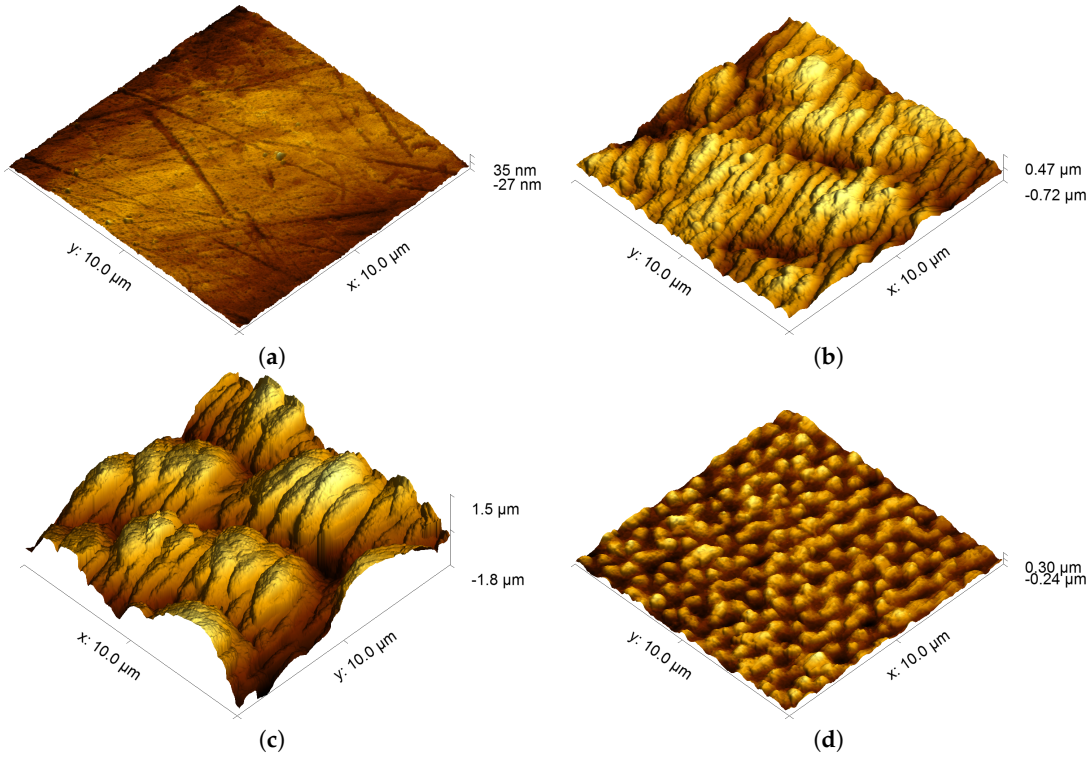


**Figure 5.** AFM micrographs of a CrCoMo surface: unprocessed (**a**), LSFL (**b**), grooves with superimposed LSFL (**c**) and triangular nanopillars (**d**). (**a**) AFM micrograph of polished CrCoMo sample. (**b**) AFM micrograph of LSFL. (**c**) AFM micrograph of Grooves + LSFL. (**d**) AFM micrograph of Triangular Nanopillars.

**Table 4.** Geometrical properties of the of the surface structures to be functionally evaluated.

| Parameter | Polished | LSFL | Grooves | TNP |
|---|---|---|---|---|
| Periodicity (nm) | - | 800 | 3550; 920 (LSFL) | 860 |
| $R_q$ (µm) | $0.004 \pm 0.0004$ | $0.163 \pm 0.029$ | $0.519 \pm 0.130$ | $0.092 \pm 0.008$ |
| $R_a$ (µm) | $0.003 \pm 0.0003$ | $0.132 \pm 0.026$ | $0.423 \pm 0.111$ | $0.077 \pm 0.007$ |
| $R_p$ (µm) | $0.010 \pm 0.007$ | $0.293 \pm 0.082$ | $1.038 \pm 0.198$ | $0.192 \pm 0.030$ |
| $R_v$ (µm) | $-0.011 \pm 0.007$ | $-0.387 \pm 0.113$ | $-0.825 \pm 0.321$ | $-0.177 \pm 0.023$ |
| $R_{sk}$ (-) | $-0.118 \pm 0.038$ | $-0.319 \pm 0.488$ | $-0.013 \pm 0.455$ | $0.038 \pm 0.216$ |
| $R_{ku}$ (-) | $0.356 \pm 0.812$ | $-0.351 \pm 0.859$ | $-0.789 \pm 0.306$ | $-0.847 \pm 0.308$ |
| $\sigma$ (-) | 1.005 | 1.328 | 1.752 | 1.307 |

As can be observed in Table 4, the dimensions of the chosen surface structures are indeed in the range of the sizes of the bacterias *S. aureus* and *E. coli*, which potentially gives these structures anti-bacterial properties [3].

### *3.4. Wetting Properties*

When anti-bacterial properties of surfaces found in nature are studied, a correlation between hydrophobicity and anti-bacterial behavior is found [2,31,32]. Since LIPSS have been found to be hydrophobic [10–15] and also anti-bacterial [15–18], hydrophobicity is used in this paper as an indication of anti-bacterial behavior.

The three surface textures (see Figure 5) show hydrophobic behavior compared to the untextured, mirror polished surface, which shows a water contact angle of ($82.7° \pm 0.7°$, see Table 5).

**Table 5.** Contact angles of chosen surface structures.

| Surface Structure | Polished | LSFL | Grooves | TNP |
|---|---|---|---|---|
| Contact angle (°) | $82.7 \pm 0.7$ | $151 \pm 2$ | $141.1 \pm 0.2$ | $133 \pm 2$ |

The LSFL surface is superhydrophobic for water, whereas the contact angle of the mirror polished CoCrMo substrate is hydrophilic. The surfaces denoted Grooves and TNP are both hydrophobic, but less so than LSFL, as is shown in Table 5. The hydrophobicity of the textured surfaces is subject to variability due to the formation of oxide layers after laser micromachining over time. The polished sample will oxidize rapidly to a protective layer of CoO, $Cr_2O_3$ and $MoO_3$ [33–36]. For example, it was shown by Huerta–Murillo et al. [37], that the contact angles of laser textured titanium alloys increase over a time period of five weeks from about 90° to 130°. The contact angles in this study were measured after seven weeks for LSFL and Grooves and after 12 days for TNP. However, a positive effect of surface texturing (irrespective of morphological class) was seen on the hydrophobic behavior of the surfaces, in line with results found in literature [12,13,15].

The influence of the surface roughness on the contact angle can be described by either Wenzel [38], where it is assumed that the total surface will be in contact with the liquid, or by Cassie [39], where different materials or a combination of trapped air and a solid will be in contact with the liquid. In case of Wenzel the relation between the apparent contact angle (CA) $\theta_a$ and the intrinsic CA $\theta_i$ is given by

$$\cos(\theta_a) = \sigma(\cos\theta_i), \tag{1}$$

where $\sigma$ is the ratio between the true surface area and the projected area. In case of hydrophilic surfaces an increase of the roughness will result in a decrease of the CA and in the case of hydrophobic surfaces an increase of the roughness will result in an increase of the CA.

In case air might be trapped due to surface morphology the contact angle according to Cassie–Baxter [39] is defined as

$$\cos(\theta_{CB}) = \sigma_{CB} f(\cos\theta_i) + f - 1. \tag{2}$$

In this equation, $\theta_{CB}$ is the apparent contact angle, $f$ is the fraction of the projected area of the surface that is wet by the liquid and $\sigma_{CB}$ is the roughness ratio of the wet area. This shows, that an increasing amount of trapped air, which means a smaller ratio $f$, will lead to an increase of the apparent contact angle.

This indicates that the measured contact angles on the CrCoMo samples due to laser processing can be explained by the increase of the ratio between the real surface area and the projected area $\sigma$ and a reduction of the wetted area due to LIPSS [40,41]. Nonetheless, the contact angles are highly dependent on the formation of additional oxide layers. Interpretation of the origin of the hydrophobic properties would require a more thorough study of this surfaces.

### *3.5. Tribological Properties*

The measured coefficient of friction (CoF) of the textured CoCrMo surfaces are listed in Table 6. The CoF of TNP with the hexagonal TNP is significantly lower than those of LSFL and Grooves. The friction coefficient of polished CoCrMo with 0.5 N (18 MPa), 11 mm/s and BCS lubricant was $0.22 \pm 0.07$. The friction coefficients of the textured surfaces are thus significantly higher than the CoF of the polished surface, due to the surface topograhphy changes.

**Table 6.** Coefficient of friction and polyethylene (PE) wear diameter of chosen surface structures.

| Surface Structure | Polished | LSFL | Grooves | TNP |
|---|---|---|---|---|
| Coefficient of friction [-] | $0.22 \pm 0.07$ | $0.66 \pm 0.05$ | $0.62 \pm 0.09$ | $0.40 \pm 0.07$ |
| PE wear diameter [mm] | $0.8 \pm 0.1$ | $3.7 \pm 0.26$ | $1.3 \pm 0.03$ | $0.8 \pm 0.04$ |

Figure 6 shows SEM micrographs of the LSFL structure after the wear test. From this figure it can be observed that the surface morphologies on the CoCrMo surface remain intact during the given wear test. After 104 min of sliding the PE sphere over the LSFL textured surface with a 18 MPa load, 11 mm/s speed and BCS lubricant, the PE ball had a volume loss of 43 $mm^3$. This is nearly 9.5% of the total sphere volume. Hence, it can be concluded that LSFL cannot be used as a bearing surface of a hip joint, since in the end of high loading, it reduces the durability of the hip joint significantly. The other two textures lead to noticeably less wear on the PE ball, see Table 6. The CoF of LSFL was also higher than that of Grooves and TNP. However, the difference between the CoF LSFL and Grooves is much smaller than the wear PE experiences against LSFL and Grooves. The fact that LSFL show a higher hydrophobicity (see Table 5) may influence the wear rate as well. High friction in a joint will lead to more heat generation, which may cause performance degradation of the joint. However, no maximally defined CoF is stated for a hip joint. The wear recorded for TNP is actually very close to that found on the polished surface.

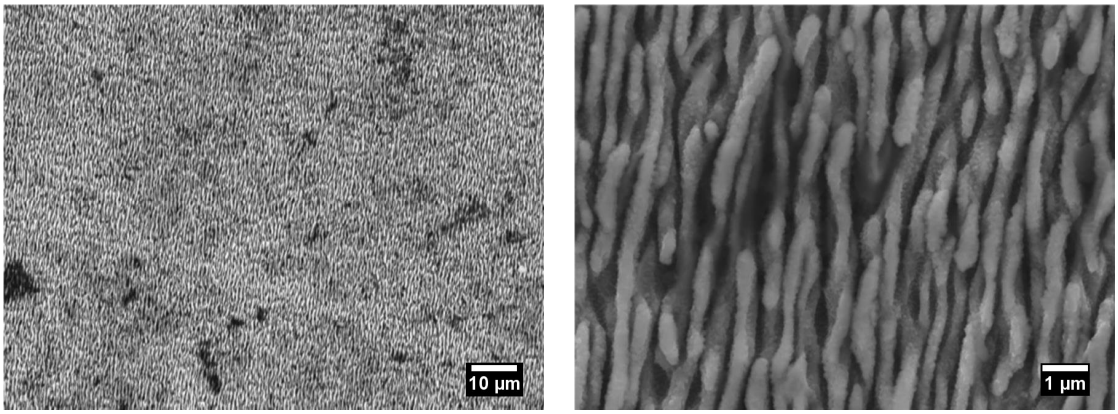


(**a**) (**b**)

**Figure 6.** SEM micrographs of LSFL structure after wear test. (**a**) SEM image LSFL. (**b**) SEM image LSFL.

The wear conditions of the UMT, which are 18 MPa, 11 mm/s, reciprocal movement, are not comparable to the wear conditions in a natural hip joint, approximately 7.8 MPa and 21 mm/s during normal gait and rotational movement in all directions [21]. Since the surface structure TNP shows a periodicity in three directions (see Figure 4), instead of one in the cases of LSFL and Grooves, and also shows the lowest CoF and PE wear very close to the polished surface, TNP is the most promising candidate for a potential anti-bacterial surface structure on an artificial hip-joint.

### *3.6. Biocompatibility*

Lutey et al. [15] showed that LSFL and TNP performed best on anti-bacterial properties regarding *E. coli* and *S. aureus* on stainless steel. A bacterial count reduction of 99.8% and 99.2% was found for *E. coli* and 84.7% and 79.9% was found for *S. aureus*, for the LSFL and TNP, respectively. Grooves (in [15] defined as Spikes) on the other hand, do not show improvement in anti-bacterial properties. However, to estimate the leaching of hazardous elements of the CoCrMo alloy into the human body, LSFL textured CoCrMo samples were used to perform a leaching test.

Release of Cobalt (Co) ions from the CoCrMo substrate may have an adverse affect on the patient's health. The Medicines and Healthcare products Regulatory Agency recommended a 7 µg/L threshold.

Concentrations above that threshold can be toxic for the patient [42]. Due to the increased surface area of the textured samples, when compared to the polished samples, textured samples may cause a higher ion release rate of Co and Ni ions. Chromium (Cr), Molybdenum (Mo) and Nickel (Ni) are also toxic in certain concentrations, but to the best of the authors knowledge no medical standardized regulations exist on acceptable concentration levels. The release of ions can be studied by means of a leaching experiment.

To that end, polished CoCrMo as well as LSFL textured CoCrMo samples were immersed in simulated body fluid (SBF, see Section 2.2.5) for nearly four weeks. Ion release was measured after 1, 7, 21 and 26 days. All samples were analyzed for the presence of Co, Cr, Mo and Ni elements by means of atomic emission spectroscopy analysis. No significant concentrations of Cr, Mo and Ni were found for any of the samples. Traces of Co were found in the SBF samples of the polished and the textured CoCrMo samples, see Figure 7. A gradual release of Co can be observed during the first two weeks for both polished and textured CoCrMo. After one day of immersion, the Co ion concentration is slightly higher for textured CoCrMo. Interestingly, there is no significant difference between the textured and untextured sample observed after one week and three weeks of immersion. After two weeks of immersion a larger Co concentration is found for polished CoCrMo and after four weeks of immersion the textured samples give a higher concentration, $27 \pm 3$ ppb vs. $17 \pm 1$ ppb. It was expected that the concentration of cobalt in the SBF would increase in time as more and more cobalt leaches from the surface into the fluid, until the equilibrium state is reached. The decrease in cobalt concentration of the untextured sample after 14 days could be explained by a change in pH due to a change in ion concentration in the SBF. The pH change could influence the equilibrium of Co ions. No precipitation of any element was observed at any point during and after the experiment. Unfortunately, the pH was not measured after the experiment. The difference in cobalt concentration after four weeks of immersion between polished and textured CoCrMo could be explained by the difference in surface area. According to Leyssens et al. [42], levels of Co lower than 300 µg/L will not cause health complications for individuals. The levels of Co in this study measured during 26 days of immersion, are well below this threshold. In the body the CoCrMo surface will be slightly larger. However, in the patients body, larger amounts of bodily fluids are present, and the human body does process low concentrations of Co [43]. However, it is questionable if this test can be compared with levels measured in patients. There are many factors which effect the leaching behavior of surfaces. To the best of our knowledge, no research on leaching of CoCrMo in SBF or similar circumstances has been conducted so far.

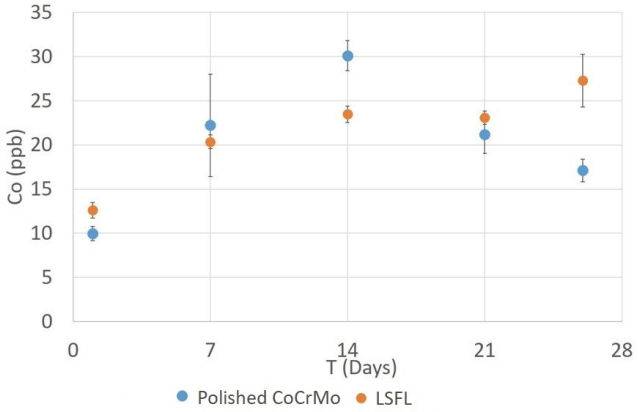


**Figure 7.** ICP-AES analysis of cobalt ion release of polished and LSFL textured CoCrMo samples in ppb as a function of time.

## 4. Conclusions

In this study, surface textures of nano and micrometer scale were produced on polished Cobalt–Chrome–Molybdenum alloy (CoCrMo) surfaces, using an infrared picosecond pulsed laser

source. It was shown that the shape and size of the surface features can be controlled by adapting the laser fluence, the number of overscans of the laser spot over the surface and the type of polarization. To evaluate the wetting, tribological and leaching properties of laser-textured surfaces, three different types of textures were homogeneously produced on a large area (larger than the laser beam diameter), namely: low spatial frequency LIPSS, hierarchical grooves with superimposed low spatial frequency LIPSS, and triangular hexagonally packed nanopillars. The tribological behavior and the wettability of these three textures on CoCrMo were compared to a polished (i.e., untextured) CoCrMo surface. It was found that the textured surfaces caused higher friction in a CoCrMo-against-PE reciprocating contact compared to a polished reference. Moreover, only the LSFL textured surface showed a significantly higher wear of the PE counter surface. Furthermore, it was found that the hydrophobicity of the surface increases significantly due the micro-machined textures. Additionally, the biocompatibility of a LSFL textured surface on CoCrMo was compared to a polished CoCrMo surface. Both polished and textured surfaces release cobalt ions over a period of four weeks, but are still well below critical threshold levels reported in literature. Although, long term leaching experiments are recommended.

Based on the experimental conditions and results of this study, it is concluded that the laser textured surfaces on CoCrMo are not suitable for bearing surfaces in a metal-on-plastic contact. It is recommended to repeat the wear experiments at lower contact pressures, comparable to the conditions found in the hip joint, to study the friction and wear of PE under realistic conditions. The wear resistance, the antimicrobial activity and the effect on human cells of the processed surface textures would have to be investigated more thoroughly. It is recommended to look into other, possibly static, applications for antibacterial LIPSS surface textures on CoCrMo, e.g., dental implants.

**Author Contributions:** Conceptualization, S.H.v.d.P.; methodology, M.M. and S.H.v.d.P.; software, M.M.; validation, M.M., E.G.d.V. and S.H.v.d.P.; formal analysis, M.M., D.T.A.M. and S.H.v.d.P.; investigation, S.H.v.d.P.; resources, all authors; data curation, M.M. and S.H.v.d.P.; writing—original draft preparation, M.M. and S.H.v.d.P.; writing—review and editing, all authors; visualization, M.M. and S.H.v.d.P.; supervision, D.T.A.M. and G.-w.R.B.E.R.; project administration, S.H.v.d.P.; funding acquisition, D.T.A.M. and G.-w.R.B.E.R.

**Funding:** Parts of this study was funded by the European Union's Horizon 2020 research and innovation programme under the Marie Skłodowska-Curie grant agreement No. 675063 (Laser4Fun project, www.laser4fun.eu).

**Acknowledgments:** We thank Soheyla Ostvar Pour, University of Manchester School of Materials, for assistance with the execution of the leaching experiment, in particular the ICP-AES analysis.

**Conflicts of Interest:** The authors declare no conflict of interest.

## Abbreviations

The following abbreviations are used in this manuscript:

| | |
|---|---|
| CoCrMo | Cobalt Chrome Molybdenum |
| PE | Polyethylene |
| LIPSS | Laser-induced periodic surface structures |
| LSFL | low spatial frequency LIPSS |
| HSFL | high spatial frequency LIPSS |
| BCS | bovine calf serum |
| FFT | Fast Fourier transformation |
| SPP | surface plasmon polaritons |
| CoF | coefficient of friction |
| SBF | simulated body fluid |
| CA | contact angle |
| ICP-AES | Inductively Coupled Plasma Atomic Emission Spectroscopy |

## References


1. Löwik, C.A.; Wagenaar, F.C.; Van Der Weegen, W.; Poolman, R.W.; Nelissen, R.G.; Bulstra, S.K.; Pronk, Y.; Vermeulen, K.M.; Wouthuyzen-Bakker, M.; Van Den Akker-Scheek, I.; et al. LEAK study: Design of a nationwide randomised controlled trial to find the best way to treat wound leakage after primary hip and knee arthroplasty. *BMJ Open* **2017**, *7*, 1–6. [CrossRef] [PubMed]
2. Jaggessar, A.; Shahali, H.; Mathew, A.; Yarlagadda, P.K. Bio-mimicking nano and micro-structured surface fabrication for antibacterial properties in medical implants. *J. Nanobiotechnol.* **2017**, *15*, 1–20. [CrossRef] [PubMed]
3. Cunha, A.; Elie, A.M.; Plawinski, L.; Serro, A.P.; Botelho Do Rego, A.M.; Almeida, A.; Urdaci, M.C.; Durrieu, M.C.; Vilar, R. Femtosecond laser surface texturing of titanium as a method to reduce the adhesion of *Staphylococcus aureus* and biofilm formation. *Appl. Surf. Sci.* **2016**, *360*, 485–493. [CrossRef]
4. Getzlaf, M.A.; Lewallen, E.A.; Kremers, H.M.; Jones, D.L.; Bonin, C.A.; Dudakovic, A.; Thaler, R.; Cohen, R.C.; Lewallen, D.G.; van Wijnen, A.J. Multi-disciplinary antimicrobial strategies for improving orthopaedic implants to prevent prosthetic joint infections in hip and knee. *J. Orthop. Res.* **2016**, *34*, 177–186. [CrossRef] [PubMed]
5. Reshes, G.; Vanounou, S.; Fishov, I.; Feingold, M. Cell shape dynamics in *Escherichia coli*. *Biophys. J.* **2008**, *94*, 251–264. [CrossRef] [PubMed]
6. Harris, L.G.; Foster, S.J.; Richards, R.G.; Lambert, P.; Stickler, D.; Eley, A. An introduction to *Staphylococcus aureus*, and techniques for identifying and quantifying *S. aureus* adhesins in relation to adhesion to biomaterials: Review. *Eur. Cells Mater.* **2002**, *4*, 39–60. [CrossRef]
7. Puccio, F.D. Biotribology of artificial hip joints. *World J. Orthop.* **2015**, *6*, 77. [CrossRef] [PubMed]
8. Smet, K.D.; Campbell, P.; Straeten, C.V.D. *The Hip Resurfacing Handbook*; Woodhead Publishing: Sawston, UK, 2013; pp. 56–58.
9. Eichstädt, J.; Römer, G.R.B.E.; Huis in't Veld, A.J. Towards friction control using laser-induced periodic Surface Structures. *Phys. Procedia* **2011**, *12*, 7–15. [CrossRef]
10. Bonse, J.; Kirner, S.V.; Koter, R.; Pentzien, S.; Spaltmann, D.; Krüger, J. Femtosecond laser-induced periodic surface structures on titanium nitride coatings for tribological applications. *Appl. Surf. Sci.* **2017**, *418*, 572–579. [CrossRef]
11. Qin, L.; Wu, H.; Guo, J.; Feng, X.; Dong, G.; Shao, J.; Zeng, Q.; Zhang, Y.; Qin, Y. Fabricating hierarchical micro and nano structures on implantable Co–Cr–Mo alloy for tissue engineering by one-step laser ablation. *Colloids Surf. B Biointerfaces* **2018**, *161*, 628–635. [CrossRef]
12. Wu, B.; Zhou, M.; Li, J.; Ye, X.; Li, G.; Cai, L. Superhydrophobic surfaces fabricated by microstructuring of stainless steel using a femtosecond laser. *Appl. Surf. Sci.* **2009**, *256*, 61–66. [CrossRef]
13. Romano, J.M.; García-Girón, A.; Penchev, P.; Dimov, S. Triangular laser-induced submicron textures for functionalising stainless steel surfaces. *Appl. Surf. Sci.* **2018**, *440*, 162–169. [CrossRef]
14. Varlamova, O.; Reif, J.; Stolz, M.; Borcia, R.; Borcia, I.D. Wetting properties of LIPSS structured silicon surfaces. *Eur. Phys. J. B* **2019**, *92*, 91. [CrossRef]
15. Lutey, A.H.; Gemini, L.; Romoli, L.; Lazzini, G.; Fuso, F.; Faucon, M.; Kling, R. Towards laser-textured antibacterial surfaces. *Sci. Rep.* **2018**, *8*, 1–10. [CrossRef]
16. Rajab, F.H.; Liauw, C.M.; Benson, P.S.; Li, L.; Whitehead, K.A. Production of hybrid macro/micro/nano surface structures on Ti6Al4V surfaces by picosecond laser surface texturing and their antifouling characteristics. *Colloids Surf. B Biointerfaces* **2017**, *160*, 688–696. [CrossRef]
17. Kunz, C.; Müller, F.A.; Gräf, S. Multifunctional hierarchical surface structures by femtosecond laser processing. *Materials* **2018**, *11*, 789. [CrossRef]
18. Fadeeva, E.; Truong, V.K.; Stiesch, M.; Chichkov, B.N.; Crawford, R.J.; Wang, J.; Ivanova, E.P. Bacterial retention on superhydrophobic titanium surfaces fabricated by femtosecond laser ablation. *Langmuir* **2011**, *27*, 3012–3019. [CrossRef]
19. The MathWorks, Inc. *MATLAB® R2015b*; The MathWorks, Inc.: Natick, MA, USA, 2015.
20. Mezera, M.; Römer, G.R.B.E. Model based optimization of process parameters to produce large homogeneous areas of laser-induced periodic surface structures. *Opt. Express* **2019**, *27*, 6012–6029. [CrossRef]
21. International Organization for Standardization. *Implants for Surgery—Wear of Total Hip-Joint Prostheses—Part 2: Methods of Measurement*; ISO 14242-2:2016; ISO: Geneva, Switzerland, 2016; pp. 1–5.

22. Kokubo, T.; Takadama, H. How useful is SBF in predicting in vivo bone bioactivity? *Biomaterials* **2006**, *27*, 2907–2915. [CrossRef]
23. Bonse, J.; Höhm, S.; Kirner, S.; Rosenfeld, A.; Krüger, J. Laser-induced periodic surface structures (LIPSS)—A scientific evergreen. *IEEE J. Sel. Top. Quantum Electron.* **2016**, *23*, 9000615.
24. Bauer, F.; Michalowski, A.; Kiedrowski, T.; Nolte, S. Heat accumulation in ultra-short pulsed scanning laser ablation of metals. *Opt. Express* **2015**, *23*, 1035. [CrossRef]
25. Faas, S.; Bielke, U.; Weber, R.; Graf, T. Prediction of the surface structures resulting from heat accumulation during processing with picosecond laser pulses at the average power of 420 W. *Appl. Phys. A Mater. Sci. Process.* **2018**, *124*, 1–9. [CrossRef]
26. Faas, S.; Bielke, U.; Weber, R.; Graf, T. Scaling the productivity of laser structuring processes using picosecond laser pulses at average powers of up to 420 W to produce superhydrophobic surfaces on stainless steel AISI 316L. *Sci. Rep.* **2019**, *9*, 1933. [CrossRef]
27. Yasumaru, N.; Miyazaki, K.; Kiuchi, J. Fluence dependence of femtosecond-laser-induced nanostructure formed on TiN and CrN. *Appl. Phys. A Mater. Sci. Process.* **2005**, *81*, 933–937. [CrossRef]
28. Assion, A.; Husinsky, W.; Ganz, T.; Kudryashov, S.I.; Ajami, A.; Ionin, A.A.; Makarov, S.V.; Nathala, C.S. Experimental study of fs-laser induced sub-100-nm periodic surface structures on titanium. *Opt. Express* **2015**, *23*, 5915.
29. Liu, Q.; Zhang, N.; Yang, J.; Qiao, H.; Guo, C. Direct fabricating large-area nanotriangle structure arrays on tungsten surface by nonlinear lithography of two femtosecond laser beams. *Opt. Express* **2018**, *26*, 11718. [CrossRef]
30. Fraggelakis, F.; Mincuzzi, G.; Lopez, J.; Manek-Hönninger, I.; Kling, R. Controlling 2D laser nano structuring over large area with double femtosecond pulses. *Appl. Surf. Sci.* **2019**, *470*, 677–686. [CrossRef]
31. Ivanova, E.P.; Hasan, J.; Webb, H.K.; Truong, V.K.; Watson, G.S.; Watson, J.A.; Baulin, V.A.; Pogodin, S.; Wang, J.Y.; Tobin, M.J.; et al. Natural bactericidal surfaces: Mechanical rupture of *Pseudomonas aeruginosa* cells by cicada wings. *Small* **2012**, *8*, 2489–2494. [CrossRef]
32. Bixler, G.D.; Theiss, A.; Bhushan, B.; Lee, S.C. Anti-fouling properties of microstructured surfaces bio-inspired by rice leaves and butterfly wings. *J. Colloid Interface Sci.* **2014**, *419*, 114–133. [CrossRef]
33. Zimmermann, J.; Colombi Ciacchi, L. Origin of the selective Cr oxidation in CoCr alloy surfaces. *J. Phys. Chem. Lett.* **2010**, *1*, 2343–2348. [CrossRef]
34. Kofstad, P.K.; Hed, A.Z. High-temperature oxidation of Co-10 w/o Cr alloys. *J. Electrochem. Soc.* **1969**, *116*, 224–229. [CrossRef]
35. Jelovica Badovinac, I.; Kavre Piltaver, I.; Peter, R.; Saric, I.; Petravic, M. Formation of oxides on CoCrMo surfaces at room temperature: An XPS study. *Appl. Surf. Sci.* **2019**, *471*, 475–481. [CrossRef]
36. Liao, Y.; Hoffman, E.; Wimmer, M.; Fischer, A.; Jacobs, J.; Marks, L. CoCrMo metal-on-metal hip replacements. *Phys. Chem. Chem. Phys.* **2013**, *15*, 1–26. [CrossRef]
37. Huerta-Murillo, D.; García-Girón, A.; Romano, J.M.; Cardoso, J.T.; Cordovilla, F.; Walker, M.; Dimov, S.S.; Ocaña, J.L. Wettability modification of laser-fabricated hierarchical surface structures in Ti-6Al-4V titanium alloy. *Appl. Surf. Sci.* **2019**, *463*, 838–846. [CrossRef]
38. Wenzel, R.N. Surface roughness and contact angle. *J. Phys. Colloid Chem.* **1949**, *53*, 1466–1467. [CrossRef]
39. Cassie, A. Contact angles. *Discuss. Faraday Soc.* **1948**, *3*, 11–16. [CrossRef]
40. Sciancalepore, C.; Gemini, L.; Romoli, L.; Bondioli, F. Study of the wettability behavior of stainless steel surfaces after ultrafast laser texturing. *Surf. Coat. Technol.* **2018**, *352*, 370–377. [CrossRef]
41. Raimbault, O.; Benayoun, S.; Anselme, K.; Mauclair, C.; Bourgade, T.; Kietzig, A.M.; Girard-Lauriault, P.L.; Valette, S.; Donnet, C. The effects of femtosecond laser-textured Ti-6Al-4V on wettability and cell response. *Mater. Sci. Eng. C* **2016**, *69*, 311–320. [CrossRef]
42. Leyssens, L.; Vinck, B.; Van Der Straeten, C.; Wuyts, F.; Maes, L. Cobalt toxicity in humans—A review of the potential sources and systemic health effects. *Toxicology* **2017**, *387*, 43–56. [CrossRef]
43. Okazaki, Y.; Gotoh, E. Comparison of metal release from various metallic biomaterials in vitro. *Biomaterials* **2005**, *26*, 11–21. [CrossRef]